Research Article

Magnetic Biochar by One-Step Impregnation Pyrolysis of Peganum harmala L. for Removal of Rhodamine B

Abdulrahman F. Alharbi,[1] Abdullah A. Alotaibi,[2,3] Hassan E. M. Gomaa,[2,3,4] Abdulaziz A. M. Abahussain,[5] and Sami M. Abdel Azeem [1,3,6]

[1]*Department of Chemistry, College of Science and Humanities, Shaqra University, Saudi Arabia*
[2]*Department of Chemistry, College of Science and Humanities, Shaqra University, 11911 Ad-Dawadmi, Saudi Arabia*
[3]*Water Research Group, College of Science and Humanities at Ad-Dawadmi, Shaqra University, Ad-Dawadmi 11911, Saudi Arabia*
[4]*Department of Nuclear Safety Engineering, Nuclear Installations Safety Division, Atomic Energy Authority, Cairo 11765, Egypt*
[5]*Department of Chemical Engineering, College of Engineering, King Saud University, P.O. Box 800, Riyadh 11421, Saudi Arabia*
[6]*Chemistry Department, Faculty of Science, Fayoum University, Egypt*

Correspondence should be addressed to Sami M. Abdel Azeem; sami_a@su.edu.sa

A new magnetic *P. harmala* biochar/Mn-ZnFe$_2$O$_4$ material was prepared by the one-step pyrolysis approach and characterized by FT-IR, SEM, XRD, and BET techniques. The efficacy of removing rhodamine B (RhB) via adsorption and catalytic degradation was examined. Adsorption removal attained 82% of $10\,mg\cdot L^{-1}$ RhB at pH 4.0, 90 min of agitation, and $3.2\,g\cdot L^{-1}$ of adsorbent. The adsorption kinetics indicated a diffusion-limited mechanism and matched the second-order model. The equilibrium data are better suited by the Langmuir isotherm, and the maximum monolayer adsorption capacity (q_{max}) was $34.5\,mg\cdot g^{-1}$. The D-R and Tempkin isotherms both showed an endothermic chemical adsorption process and negligible lateral repulsive forces, respectively. The catalytic removal by Fenton-like degradation was 40 and 99%, respectively, for the biochar/H$_2$O$_2$ and biochar/Mn-ZnFe$_2$O$_4$/H$_2$O$_2$. The prospective use of *P. harmala* biochar/Mn-ZnFe$_2$O$_4$ as an alternative material for RhB decontamination of water was validated by the successful removal of RhB from industrial wastewater of greater than 77% by adsorption and of 95% by the catalytic degradation.

1. Introduction

The reuse of water after pollutant removal is one of the most serious environmental concerns. When a toxic substance enters the water, its quality deteriorates. Dyes are a major source of pollution, particularly in water treatment. Several synthetic organic dyes are widely used and essential in a variety of industries. Dye-contaminated effluent disposal can seriously pollute surface and groundwater [1]. This is because most dyes are toxic and endanger human health. The level of contamination by a specific dye distinguishes its true application. Rhodamine B (RhB) dye, for example, is widely used in the textile, food, cosmetics, and pharma-ceutical industries [2, 3]. Huang et al. [4] disclosed the high toxicity in a body of water as a result of RhB disposal. Congenital diseases and cancer are among the health risks posed by RhB in water [5, 6]. The removal of RhB dye from water can be accomplished through catalytic degradation and/or adsorption. Several materials have been developed for the catalytic and adsorption removal of RhB. Among these catalysts are Ti/Ru$_{0.3}$Ti$_{0.7}$O$_2$ [3], iron-doped mesoporous silica [7], nanozero valent iron (nZVI)@biochar [8], and TiO$_2$-AuNP/polydimethylsiloxane sponge [9], which were reported. RhB adsorbent materials include zinc ferrite-polyaniline [1], activated pine cone [10], stalk corn-activated carbon [11], Argemone mexicana [12],

bentonite-titanium dioxide composites [13], graphene oxide/silicalite-1 composites [14], carbon xerogels [15], and modified alpha-alumina [16]. When biomass is heated to a point of thermal breakdown without oxygen, a material called biochar is created that is rich in carbon and has fine grains. The solid biochar itself, the liquid biooil, and the syngas are the three byproducts of pyrolysis. Temperature, heating rate, and residence duration all affect the biochar's characteristics [17]. A variety of biochars were made for RhB adsorption using a variety of materials, including macroalgae [18], olive waste biomass [19], goat manure [20], and cocoa pod husk [21]. Due to their high surface-to-volume ratio, superparamagnetic characteristics, and nanoscale size, several ferrite nanoparticles have been applied to the filtration of water. However, one of the fundamental issues with these nanomaterials' actual usage as adsorbents is their tendency to aggregate. As a result, they are frequently combined with polymers to create nanocomposites that can be utilized as adsorbents. The spinel ferrites have the chemical formula $MeFe_2O_4$, where Me stands for many metals that can be included in the ferrite lattice, including Mg, Ni, Cu, Mn, Co, and Zn. These metal-based ferrites are frequently employed for adsorption research because of their strong magnetic permeability and chemical stability [22]. In environmental purification processes, magnetic biochar has the potential to be used as an adsorbent, catalyst, or soil remediation agent. This is due to the fact that its magnetic separation capabilities make it possible to easily recover pollutants and/or adsorbents from water, rendering it an environmentally safe material. Additionally, the combination of magnetic nanomaterial and biochar results in high adsorption efficiency. Many magnetic biochars have been described as adsorbents, including banana peel biochar/Fe_3O_4 [23], ferric and biological sludge biochar [24], and *Eichhornia crassipes*/Fe_3O_4 [25].

In this study, we sought to prepare a new magnetic biochar/$Mn-ZnFe_2O_4$ of the *Peganum harmala* plant for the adsorption removal and catalytic degradation of RhB dye in water. The adsorption performance and removal efficiency of RhB dye from aqueous solutions will be evaluated. Also, the application of the new adsorbent in real water will be studied.

2. Experimental

2.1. Instrumentation. The spectrophotometric measurements of RhB dye were made using a Cintra 1010 double-beam UV-Vis spectrophotometer and Cintra 2.4 software (GBC Scientific Equipment, Braeside, Australia) at a fixed wavelength of 554 nm. For the pyrolysis process, a Nabertherm vacuum muffle furnace model B180 (Lilienthal, Germany) with a protective gas connection and a programmed furnace controller with a temperature range of 30-3000°C was used. The FT-IR spectra of the *P. harmala* biochar/$Mn-ZnFe_2O_4$ were recorded in the wavenumber range of 400–4000 cm^{-1} using a Fourier transform infrared spectrometer (Perkin Elmer 1750, MA, USA) using the KBr discs technique.

On the Bruker D8 Advance diffractometer (Berlin, Germany), an X-ray diffraction (XRD) pattern was captured using Cu-K1 anode radiation at 1.54058 and a secondary monochromator. To determine the phase composition and average crystallite size of the magnetic nanoparticles, the scanning speed was set at 1° min^{-1}. The surface area and porosity were determined using the fully automated Micromeritics® TriStar II Plus analyzer model 2390t V2.03 (GA, USA). At 77 K and a relative pressure (P/Po) in the range of 0.0586–0.996, N_2 was adsorbed and then desorption. Before measurement, the samples were degassed at 120°C for two hours. The specific surface area and total pore size were determined using the Brunauer-Emmett-Teller (BET) and the Barrett-Joyner-Halenda (BJH) models. The SEM micrograph of the surface morphology of the prepared magnetic biochar was performed on JEOL scanning electron microscope (MA, USA). A Jenway bench pH meter model 4510 (Keison International Ltd., Chelmsford, UK) was used to test the pH of the samples, and it was calibrated using buffer solutions of pH 4 and 9. Stuart orbital mechanical shaker model S1500 (London, UK), with a speed of 30-300 rpm, was used to agitate the samples. Hamilton water purification system (Hamilton Glass Ltd., Margate, UK) provided double-distilled water for the duration of the study. For all filtering purposes, qualitative filter paper No. 101 (Dorsan Filtration SL Co., Barcelona, Spain) was used. Glass bottles with Teflon caps were used for the adsorption study.

2.2. Reagents. All reagents used were of analytical reagent grade, and the standard solutions were prepared in DDW. The standard RhB solution was prepared using rhodamine B dye purchased from Suvachem Co. (Maharashtra, India). Manganese chloride ($MnCl_2$), zinc chloride ($ZnCl_2$), and ferric chloride nonahydrate $FeCl_3 \cdot 9H_2O$, from Alpha Chemika™ (Mumbai, India), and sodium hydroxide (NaOH), from Sigma-Aldrich, were used to prepare the magnetic nanoparticles. By taking the appropriate amount of the reagent, a stock solution of 1000 mg·L^{-1} RhB was prepared. The working RhB concentration of 10 mg·L^{-1} was obtained by diluting the stock solution with double-distilled water.

2.3. Preparation of P. harmala Biochar/$Mn-ZnFe_2O_4$. It was decided to employ Mn and Zn in the magnetic biochar's ferrite since $Mn-ZnFe_2O_4$ is one of the most prevalent soft ferrites. These ferrites are favored because of their good stability, high saturation magnetization, and high permeability. This establishes them as well-known and popular materials for catalysis and wastewater treatment. The one-step impregnation pyrolysis method was applied to prepare the *P. harmala* biochar/$Mn-ZnFe_2O_4$ adsorbent. According to the modified method [26], the *P. harmala* powder was dried at 105°C for 24 h and sieved to 0.1 mm. A 100 mL chemical solution of the nanoparticle precursor was prepared by mixing 30 mL of 0.25 mol·L^{-1} $MnCl_2$, 20 mL of 0.25 mol·L^{-1} $ZnCl_2$, and 50 mL of 0.5 mol·L^{-1} $FeCl_3$ solution to get molar ratios of 0.6 : 0.4 : 2.0 from Mn^{2+}, Zn^{2+}, and Fe^{3+}, respectively. Then, 10 g of the plant powder was added to the above solution and mechanically stirred for 2 h. Thereafter, 50 mL of 10 mol·L^{-1} sodium hydroxide was added dropwise, and
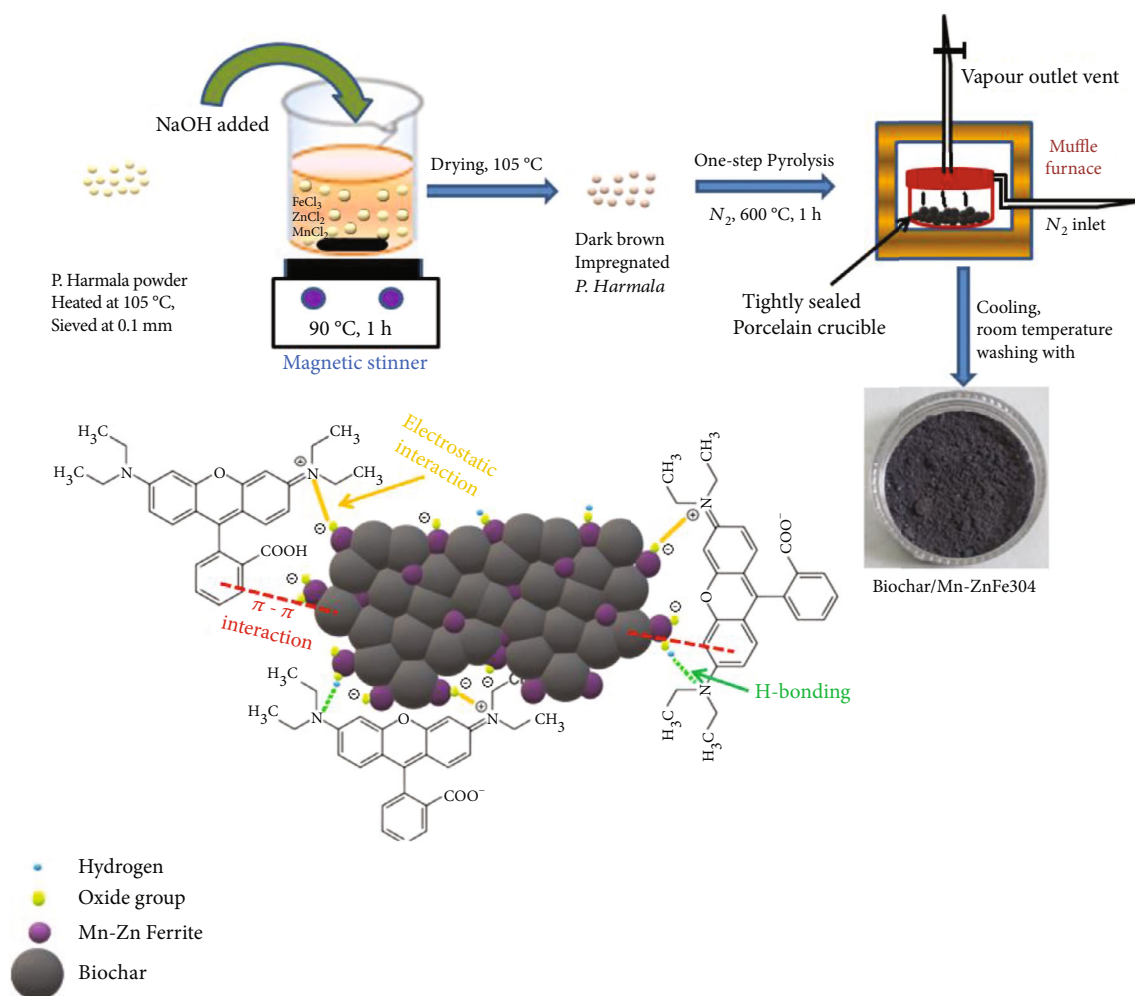
FIGURE 1: One-step impregnation synthesis protocol of *P. harmala* biochar/Mn-ZnFe$_2$O$_4$.

the slurry was heated to 90°C for one hour till a viscous gelatinous solution was formed. The resulting gel material was placed in a tightly sealed and cleaned porcelain crucible and pyrolyzed under an N$_2$ atmosphere in the NABER/B180 furnace for one hour at a setting temperature of 600°C and a heating rate of 10°C·min^{-1} from 100 to 600°C. Further, the magnetic biochar was cooled at room temperature, immersed in 0.1 mol·L^{-1} HCl solution under stirring for one hour, washed with double-distilled water to effluent that was barely neutral, and then dried, milled, and stored for further use. A ferrite with the chemical formula Mn$_{0.6}$Zn$_{0.4}$Fe$_2$O$_4$ is produced using these molar ratios of the metal ions, which is referred to as Mn-ZnFe$_2$O$_4$ throughout this study. A schematic diagram of the synthesis protocol and adsorption mechanisms is shown in Figure 1. Similarly, the *P. harmala* biochar was produced by direct pyrolysis of plant powder at a temperature of 600°C for 1 hour.

The point of zero-electric charge (pH$_{PZC}$) of *P. harmala* biochar/Mn-ZnFe$_2$O$_4$ was determined using the potassium chloride solid addition method [27]. For this purpose, a total of 50 mL of 0.1 mol·L^{-1} KCl portions was adjusted to pH 2, 4, 6, 8, and 10. Each solution was fed with 100 mg of the mag-

netic biochar, and the pH was measured both immediately and after 24 h. By plotting the pH change (ΔpH) versus the initial pH, the intersection point of the line at ΔpH = 0 is taken as the value of pH$_{PZC}$.

2.4. Adsorption Procedure. The removal of RhB dye was investigated using a 10 mL solution containing 10 mg·L^{-1} and 50 mg adsorbent and shaking for time intervals ranging from 2 to 100 minutes at 250 rpm at room temperature. The effect of pH on dye removal was studied from 1.0 to 9.0 using 0.1 mol·L^{-1} solution of HCl or NaOH for adjustment. The adsorbent dose was investigated from 0.2 to 5.0 g·L^{-1}. The initial concentration of RhB was examined from 5.0 to 100 mg·L^{-1}. After the adsorption process, the adsorbent was collected by the magnet, and the remaining dye was measured. For dye quantification, a calibration curve was created by plotting the absorbance (A) of RhB standard solutions at concentrations (C) ranging from 0.1 to 10.0 mg·L^{-1} and measured at λ_{max} 554 nm. The resulting regression equation was $A = 0.068\,C + 0.002\,(R^2 = 0.992)$.

With C_0 and C representing the initial and remaining dye concentrations (mg·L^{-1}), V for the sample volume (L),
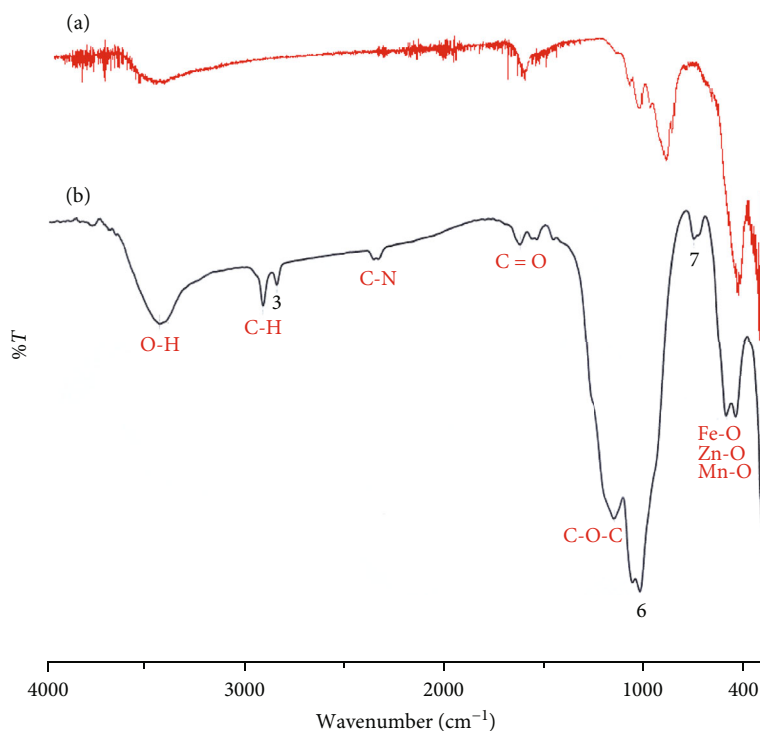
FIGURE 2: FT-IR spectra of untreated the *P. harmala* biochar (a) and biochar/Mn-ZnFe$_2$O$_4$ (b).

and m for the adsorbent weight (g), the RhB removal (%) was calculated using the following equation:

$$\text{Removal (\%)} = \left[\frac{C_0 - C}{C_0}\right] \times 100. \quad (1)$$

Also, the adsorbent RhB amount at equilibrium (q_e, mg·g^{-1}) could be calculated by using

$$q_e = \frac{[(C_0 - C) \times V]}{m}. \quad (2)$$

2.5. Catalytic Degradation Procedure. For the catalytic degradation of RhB, the heterogeneous Fenton-like degradation approach was examined. Four trials on RhB removal were conducted in accordance with the reported method [23] using the following materials: P. harmala biochar alone, P. harmala biochar and H$_2$O$_2$, biochar/Mn-ZnFe$_2$O$_4$ alone, and biochar/Mn-ZnFe$_2$O$_4$ and H$_2$O$_2$. When utilizing the biochar alone or the biochar/Mn-ZnFe$_2$O$_4$, 50 mg of the substance was added to 20 mL of a 10 mg·L^{-1} RhB solution. The removal efficiency was measured following a pH 4.0 adjustment and 90 min of shaking. The mixture for the P. harmala biochar/H$_2$O$_2$ or P. harmala biochar/Mn-ZnFe$_2$O$_4$/H$_2$O$_2$ combinations was made by combining 50 mg of the material with 20 mL of 10 mg·L^{-1} RhB solution, followed by the addition of a 0.5 mL aliquot of 1.2% (*v/v*) H$_2$O$_2$, yielding a final H$_2$O$_2$ concentration of 0.03% (*v/v*). The resulting mixture was similarly adjusted to pH 4.0 and agitated for 90 min before the remaining dye concentration was measured using the suggested technique.

3. Results and Discussion

3.1. Characterization of Biochar/Mn-ZnFe$_2$O$_4$. Figure 2 depicts the obtained FT-IR spectra of the biochar alone and the biochar/Mn-ZnFe$_2$O$_4$. A characteristic absorption band at 551 cm^{-1} corresponded to the interaction between metal and oxygen ions that occurred in the tetrahedral and octahedral positions in the spinel crystal lattice of ferrite [28]. A weak absorption peak at 1702, 2334, and 2941 cm^{-1} were assigned for the C=O, C-N, and C-H stretching vibrations of the aromatic compounds in the biochar. Also, the broad absorption band ranged from 3200 to 3640 cm^{-1} corresponding to the O-H stretching vibration of metal-OH. As a result, this confirmed that both characteristics of the *P. harmala* biochar and the impregnated Mn-ZnFe$_2$O$_4$ nanoparticles are depicted in the FT-IR spectrum. Characteristic bands for the negatively charged metal oxide groups of Fe-O, Zn-O, and Mn-O appeared at 543 and 591 cm^{-1}.

The morphological microstructure of the prepared *P. harmala* biochar/Mn-ZnFe$_2$O$_4$ was investigated using SEM analysis. The SEM analysis for determining the morphological surface structure is shown in Figure 3. The prepared magnetic biochar has an amorphous microstructure, and the stuffing Mn-ZnFe$_2$O$_4$ nanoparticles were randomly dispersed over the carbon of the biochar surface as white spots. The rough and irregular microstructure of the surface also indicates surface heterogeneity.

Figure 4 shows the XRD pattern of the developed *P. harmala* biochar/Mn-ZnFe$_2$O$_4$. The profile of the material contains a broad peak around 10-30° corresponding to the cellulose crystal. Also, a small peak was observed at 43° which is typical of graphite [29]. Moreover, the characteristic
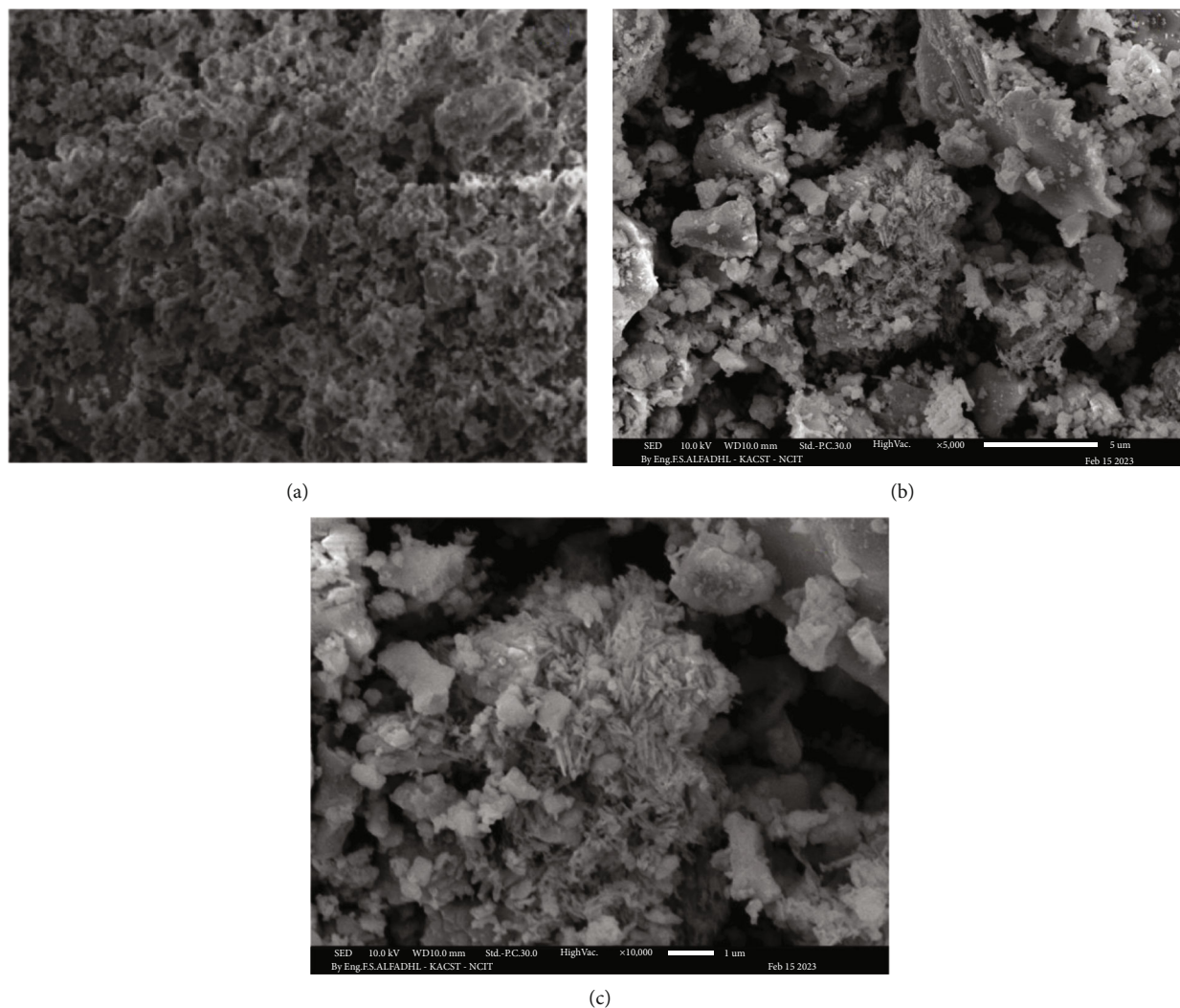
(a)

(b)

(c)

FIGURE 3: SEM micrographs for *P. harmala* biochar alone (a), biochar/Mn-ZnFe$_2$O$_4$ at 500x (b), and biochar/Mn-ZnFe$_2$O$_4$ at 10000x (c).

peaks for Fe$_3$O$_4$ nanoparticles were clearly distinguished by peaks at 2Θ of 29.71°, 34.99°, 36.60°, 42.51°, 52.73°, 56.20°, 61.70°, and 72.94°, which correspond to the (220), (311), (222), (400), (422), (511), (440), and (533) planes. This indicates that the prepared magnetic biochar has the same crystal planes as both ZnFe$_2$O$_4$ and MnFe$_2$O$_4$ according to the XRD JCPDS (Joint Committee on Powder Diffraction Standards) data files No. 22-1012 and No. 74-2403, respectively [30].

The surface area and porosity of magnetic biochars derived from a plant that is open to interaction with RhB are determined by the plant's initial composition and structure, the activation method used, and the agents used. The isotherm profile of N$_2$ adsorption-desorption on the developed adsorbent is shown in Figure 5. The multipoint BET model at a relative pressure (P/Po) from 0.058 to 0.274 was used to determine the surface area of the prepared biochar/Mn-ZnFe$_2$O$_4$. The specific surface area (S_{BET}) before adsorption was 3.605 m^2·g^{-1}. The profile exhibited type III adsorption-desorption isotherm, indicating that the adsorbent has a wide range of pore sizes [31]. This confirmed the simultaneous formation of the monolayer, bilayer, trilayer, and other layers with an exponential rising in the adsorbed dye amount. The pore size distribution presented in Figure 6 showed that the obtained material was mesoporous and macroporous. The cumulative pore volume and average pore size ($4V_{total}/S_{BET}$) calculated by the BJH method were 0.0178 cm^3·g^{-1} and 28.58 nm, respectively.

3.2. Adsorption Removal

3.2.1. Effect of pH. The effect of pH on the adsorption of RhB dye is a significant parameter since it can alter the ionic form of the dye as well as the surface charge of the adsorbent. As can be seen in Figure 7(a), the removal was higher than 82% at pH 2-5 and then rapidly decreased from 80 to 15% at pH 6-10. As a result, pH 4 was chosen as the appropriate value. As shown in Figure 7(b), the estimated value of pH$_{PZC}$ was found to be pH 6.3. This means that the surface is positively charged at a pH less than pH$_{PZC}$. RhB has a pKa of 3.7, indicating that the cationic form predominates at pH below 3.7 and the zwitterionic form predominates above pH 3.7 [32].

Interpretation of higher removal at lower pH values can be due to the adsorbent surface being positively charged and the dye existing in the cationic and the zwitterions forms. At
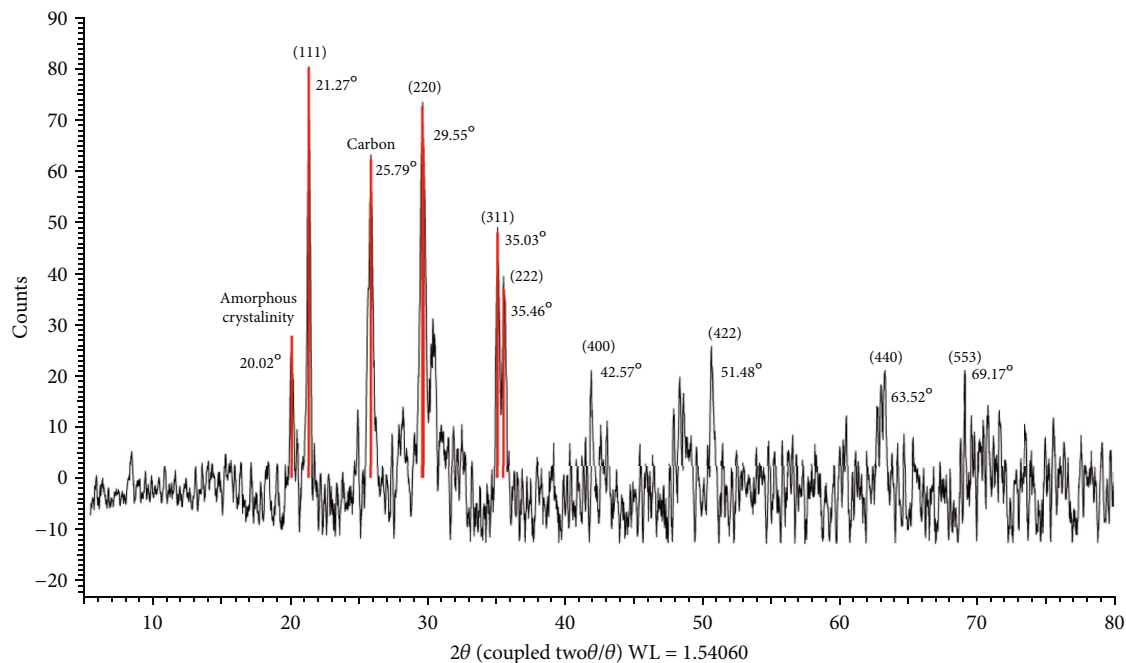
FIGURE 4: XRD pattern of the prepared *P. harmala* biochar/Mn-ZnFe$_2$O$_4$.
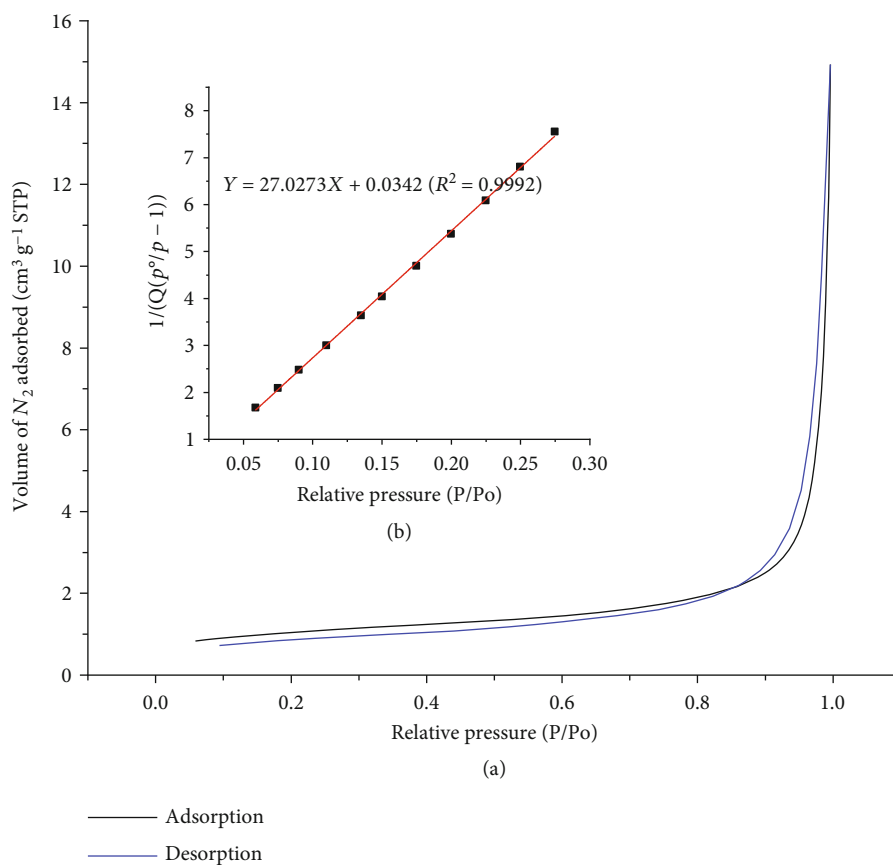
FIGURE 5: The N$_2$ adsorption-desorption isotherm of *P. harmala* biochar/Mn-ZnFe$_2$O$_4$ (a) and multipoint BET isotherm model (b).

pH less than 6.3, electrostatic attraction and the hydrophobic-hydrophobic (π-π) adsorption processes are the two basic adsorption mechanisms that might take place.

In this situation, the hydrophobic aromatic portion of the dye forms a π-π bond with the carbon in the biochar as the negative anionic COO$^-$ groups in RhB bind to the

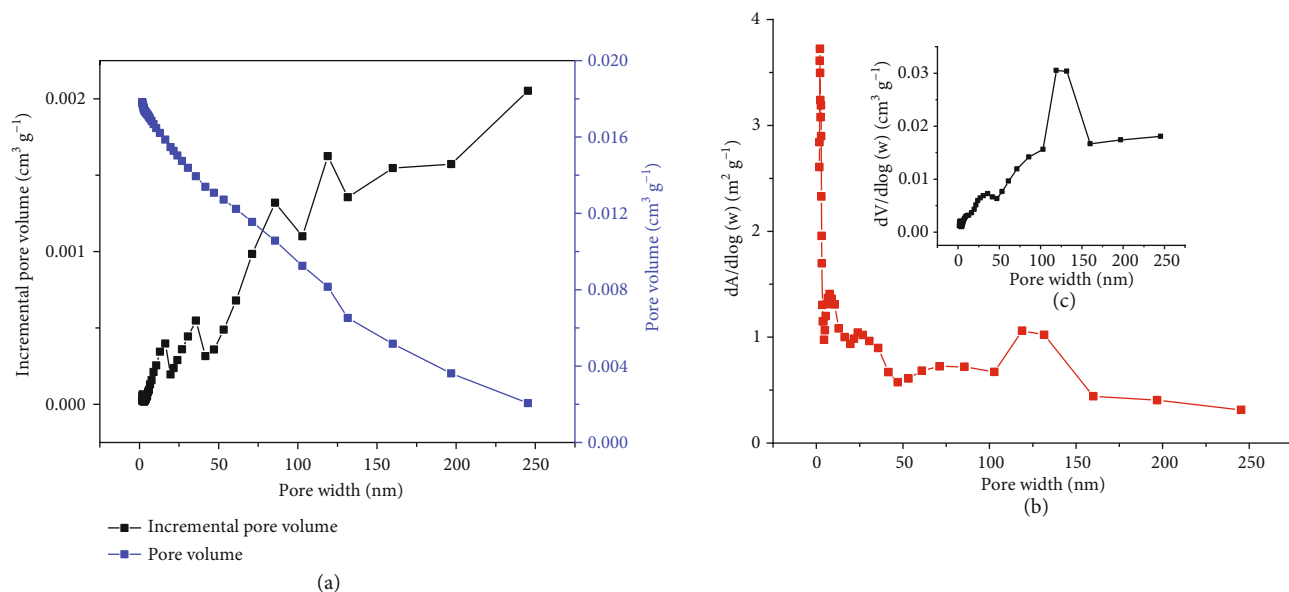Figure 6: Variation of pore volume and incremental pore volume with pore width (a). The BJH model of pore area (b) and pore volume (c) with pore width of *P. harmala* biochar/Mn-ZnFe$_2$O$_4$.
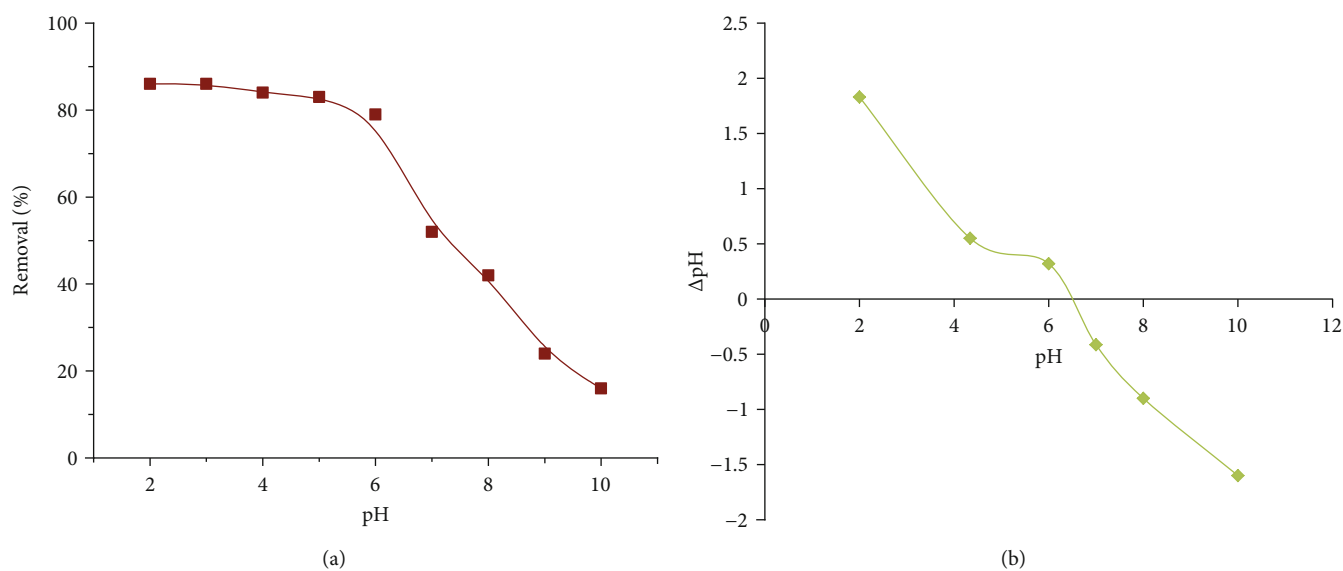

Figure 7: Effect of pH on RhB removal by *P. harmala* biochar/Mn-ZnFe$_2$O$_4$ (a) and determination of the point of zero-electric charge (b): RhB (10 mg·L^{-1}), sample volume of 20 mL, adsorbent weight 100 mg, and shaking time of 100 min.

positive surface [33]. This can be divided into two stages. At pH less than 3.7, the hydrophobic-hydrophobic interaction between the hydrophobic carbon skeleton in the biochar and the aromatic moiety of RhB would be efficient when both the dye and the adsorbent are positively charged. The hydrophobic interaction mechanism currently has the upper hand. The electrostatic attraction takes over in the pH range of 3.7 to 6.3 as the negatively charged carboxylic group (COO$^-$) in the dye's zwitterionic form strongly attracts the positively charged protonated OH groups in the ferrite. Notably, the removal remained higher than 80% even at a pH of 6.0, showing that the dye's conversion to its zwitterionic form at pH 3.7 involved an electrostatic interaction that contributed to adsorption and the pH's ability to coun-

teract the loss of hydrophobic-hydrophobic attraction. As a result, it is anticipated that electrostatic interaction will rule at pH values between 3 and 6.0. The removal decreased quickly at pH > 6.0, possibly because the ferrite OH groups had changed into negatively charged oxygenates [34]. This caused the adsorbent surface to become negatively charged, repelling the dye's negatively charged carboxylic groups. Furthermore, in moderately acidic to neutral media where the OH groups of the ferrite are not protonated or ionized, hydrogen bonding can contribute to dye adsorption. It is important to note that the dye appears in monomeric form in acidic conditions, which is smaller and more easily absorbed. Controversially, in an alkaline solution, RhB monomers' intermolecular electrostatic attraction to negatively
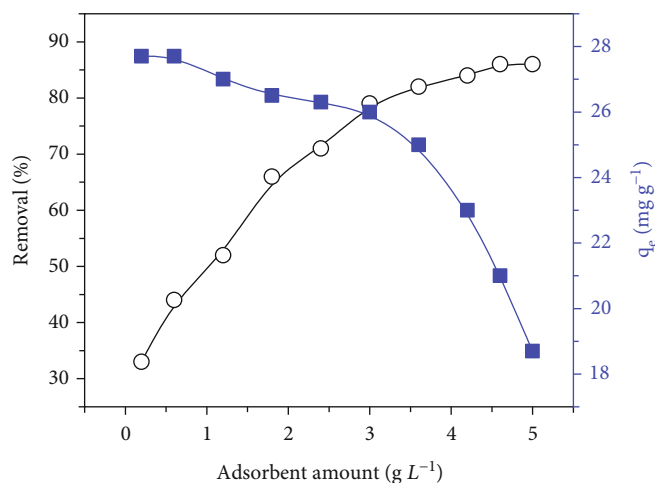
FIGURE 8: Effect of *P. harmala* biochar/Mn-ZnFe$_2$O$_4$ dosage on the adsorption of RhB (10 mg·L^{-1}), pH 4, sample volume of 20 mL, and shaking time of 100 min.
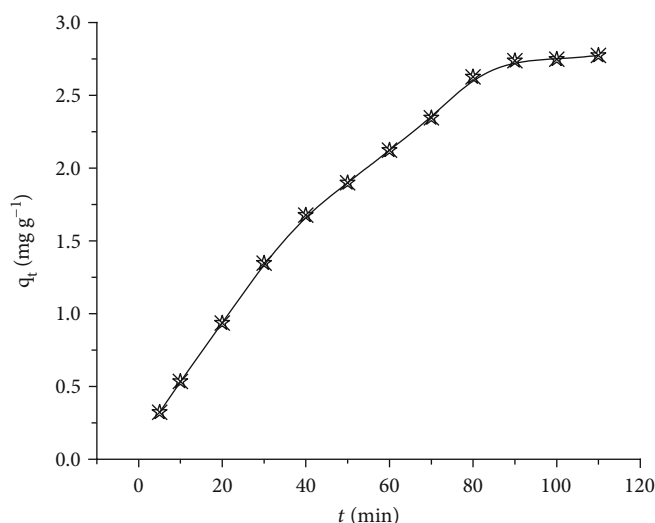

FIGURE 9: Effect of shaking time on the *P. harmala* biochar/Mn-ZnFe$_2$O$_4$ adsorption of RhB (10 mg·L^{-1}), pH 4, sample volume of 20 mL, and adsorbent weight 50 mg.

charged COO$^-$ and xanthene groups results in the creation of larger dimer aggregates that are difficult to diffuse into adsorbent pores and, as a result, to adsorb. The quick decline in removal in an alkaline media may be caused by the hydrogen bonding interaction to polar surface groups. But the massive dye aggregates could not be adsorbed by this force. Finally, pH 4.0 was chosen as the ideal value for the adsorption investigation to be lower than pH$_{PZC}$, which is advised for cationic removals, such as RhB dye in this instance.

3.2.2. Adsorbent Dose.

The impact of adsorbent dosage on removal effectiveness and adsorbed amount (q_e) was investigated due to the financial implications. The adsorbent dosage was examined from 0.2 to 5.0 g·L^{-1} at a dye concentration of 10 mg·L^{-1}. Figure 8 shows the results obtained. Steadily, the removal (%) increased as the dosage increased from 0.2 to 4.6 g·L^{-1} and reached a maximum removal of 86% afterward. No substantial change in the removal efficiency was observed

beyond 4.6 g·L^{-1}. This could be because the higher adsorbent amount increases the number of active sites accessible for adsorption, leading to efficient dye removal [35]. In contrast, the adsorbed amount (q_e) decreased by increasing the adsorbent dose which can be due to the incomplete saturation of the adsorbent surface with the necessary amount of dye as a higher adsorbent amount can prevent the dye molecules from accessing the available active sites on the adsorbent surface. According to this profile, even if the dose is raised after the ideal adsorption condition is obtained at a particular dosage, the leftover RhB dye concentration remains constant. The intersection of the two curves was discovered at 3.2 g·L^{-1}, which is regarded as the ideal adsorbent dose when comparing removal effectiveness and price.

3.2.3. Initial RhB Concentration.

The influence of initial dye concentration on removal efficiency and the adsorbed amount was examined at dye concentrations ranging from
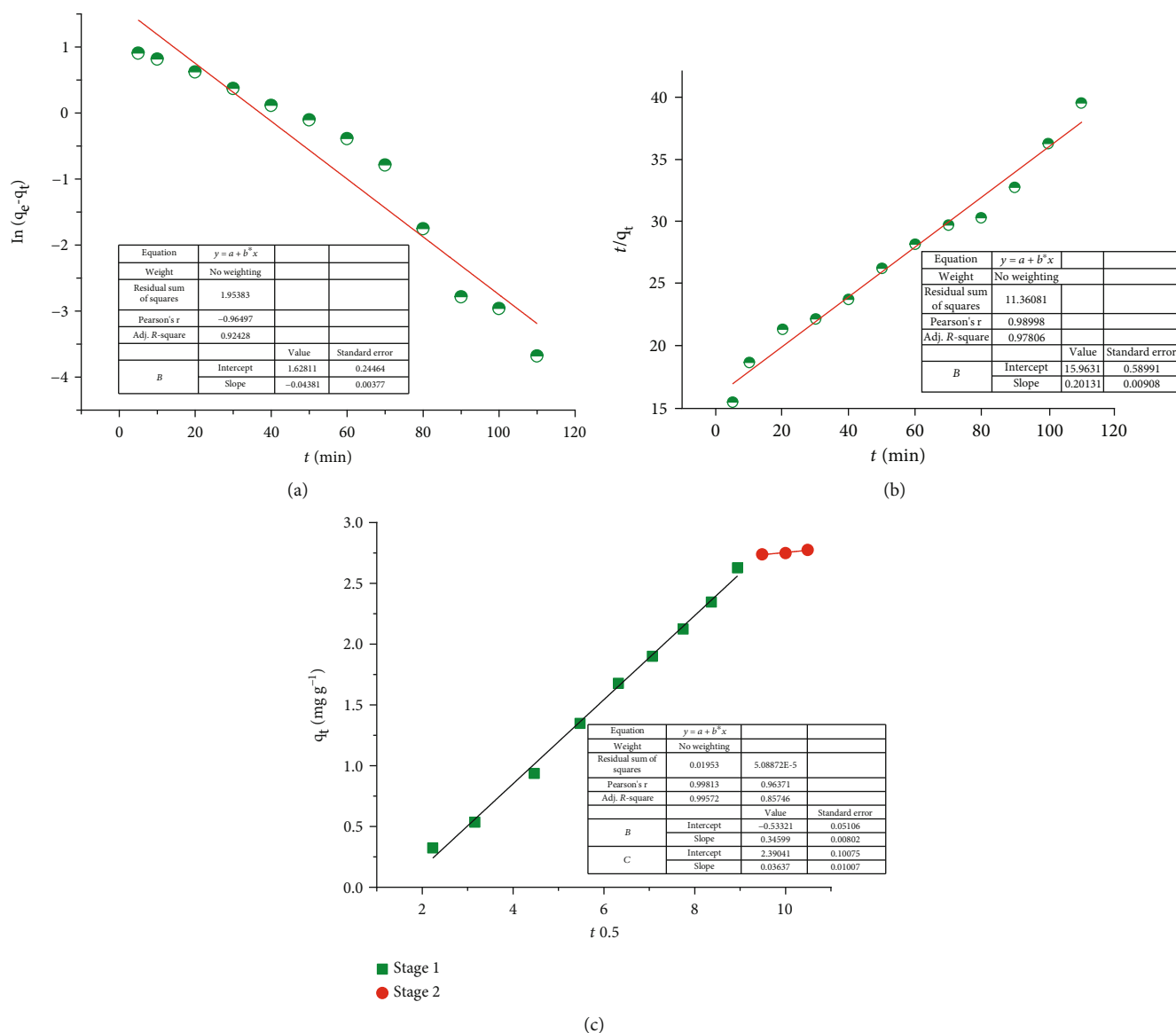
Equation	$y = a + b^*x$	
Weight	No weighting	
Residual sum of squares	1.95383	
Pearson's r	−0.96497	
Adj. R-square	0.92428	
		Value	Standard error
B	Intercept	1.62811	0.24464
	Slope	−0.04381	0.00377

(a)

Equation	$y = a + b^*x$	
Weight	No weighting	
Residual sum of squares	11.36081	
Pearson's r	0.98998	
Adj. R-square	0.97806	
		Value	Standard error
B	Intercept	15.9631	0.58991
	Slope	0.20131	0.00908

(b)

Equation	$y = a + b^*x$	
Weight	No weighting	
Residual sum of squares	0.01953	5.08872E-5
Pearson's r	0.99813	0.96371
Adj. R-square	0.99572	0.85746
		Value	Standard error
B	Intercept	−0.53321	0.05106
	Slope	0.34599	0.00802
C	Intercept	2.39041	0.10075
	Slope	0.03637	0.01007

■ Stage 1
● Stage 2

(c)

FIGURE 10: Pseudo-first-order (a), pseudo-second-order kinetic (b), and intraparticle diffusion (c) kinetic models.

5 to 100 mg·L^{-1} to compute the experimental adsorption capacity (q_{exp}) and apply isotherm models. The removal (%) was strongly dependent on the initial concentration and gradually declined by increasing the dye concentration. The gradual decrease in removal could be caused by raising the dye concentration above the adsorbent capacity, which causes the amount of the remaining dye to gradually increase. As the initial concentration rose, the amount adsorbed rose quickly until it roughly reached its maximum at 80 mg·L^{-1}, which matched an experimental adsorption capacity (q_{exp}) of 27.7 mg RhB·g^{-1}.

3.2.4. Adsorption Removal Kinetics. The time effect on removal justifies the use of this magnetic biochar in terms of the rate at which the dye can transfer from the aqueous phase to the solid adsorbent. The agitation period was examined over a while of 5 to 110 min. Figure 9 depicts the results obtained for

the variation of the adsorbed amount q_t (mg·g^{-1}) at any time t. The uptake was rapid within the first 40 min, with more than 50% of the adsorbed amount achieved. After this, adsorption increased at a slower rate, reaching equilibration and maximum adsorption after 90 min. The early quick adsorption shows how easily RhB may be removed using the adsorbent material. This verifies the strong binding force between the dye ions and the adsorbent substance, indicating that it is important for the removal process. Finally, the shaking time in subsequent experiments was set at 90 min to ensure equilibration and quantitative adsorption.

By comparing the fit of experimental results to the pseudo-first-order, pseudo-second-order, and intraparticle diffusion models, the mechanism that controls adsorption kinetics was investigated. Given that q_e and q_t represent the amount of RhB adsorbed (mg·g^{-1}) at equilibrium and at any time t (min), respectively, the pseudo-first-order rate

TABLE 1: Adsorption kinetic data for RhB dye adsorption onto P. harmala biochar/Mn-ZnFe$_2$O$_4$.

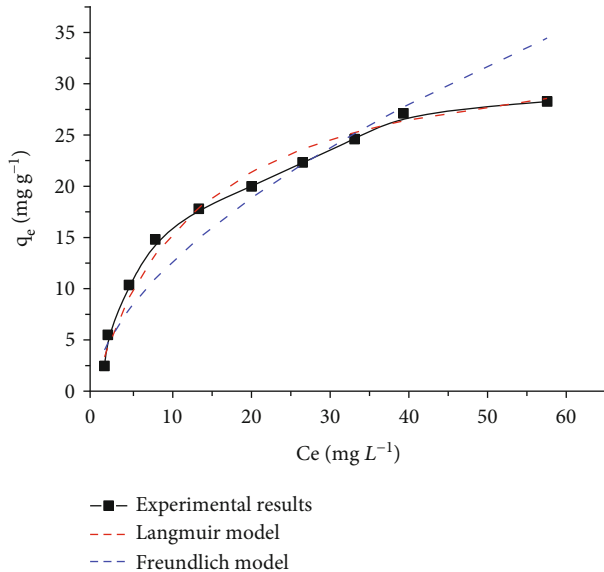| Pseudo-first-order model				Pseudo-second-order model			Intraparticle diffusion	
q_e, q_{exp} (mg·g^{-1})	q_e (mg g^{-1})	K_1 (min^{-1})	R^2	q_e (mg·g^{-1})	K_2 (g·mg^{-1}·min^{-1})	R^2	k_{id} (mg·g^{-1}·min$^{1/2}$)	R^2
2.77	5.09	0.044	0.924	4.71	0.003	0.978	0.346	0.995

FIGURE 11: Experimental equilibrium data and the fitting to the Langmuir isotherm and Freundlich isotherm models: RhB concentration 5-100 mg·L^{-1}, pH 4, sample volume of 20 mL, P. harmala biochar/Mn-ZnFe$_2$O$_4$ adsorbent weight 50 mg, and shaking time 90 min.

model of Lagergren and Kungliga [36] is shown as follows:

$$\log (q_e - q_t) = \log q_e - \frac{k_1 t}{2.303}. \tag{3}$$

Plotting $\log (q_e - q_t)$ versus t could be used to test the validity of the pseudo-first-order model.

The pseudo-second-order suggested by Ho et al. [37] is expressed by

$$\frac{t}{q_t} = \frac{1}{K_2 \cdot q_e^2} + \frac{1}{q_e} t, \tag{4}$$

where k_2 is the pseudo-second-order rate constant (μg·g^{-1}·min^{-1}).

Figures 10(a)–10(c) display the plotting of these models. Additionally, Table 1 includes the collected kinetic data. A higher linear correlation coefficient (R^2) is found in the regression analysis results of the pseudo-second-order model than in the pseudo-first-order one. Additionally, compared to the pseudo-first-order model, the computed q_e value for the pseudo-second-order model was closer to the experimental value. Therefore, the pseudo-second-order model is more suitable to describe the experimental results. This shows that the characteristics of the dye and the adsorbent surface groups both affect the adsorption process. The

Morris-Weber model [38] of the intraparticle diffusion behavior is given by Equation (5). The intraparticle diffusion rate constant k_{id} (mg·g^{-1}·min$^{-1/2}$) was calculated using the slope of the plot of q_t values versus the square root of time t.

$$q_t = k_{id} t^{1/2} \tag{5}$$

A multistep adsorption mechanism was implied by a linear relationship with a steeper slope at beginning intervals, followed by a second linear range with a lower slope, as depicted in Figure 10(c). It was also proposed that a film diffusion phase occurred during the initial adsorption stages, which were indicated by straight lines that did not pass through the origin. Thus, intraparticle diffusion contributes to the rate-limiting step. With an R^2 value of 0.996, a strong connection was found at the first stage, demonstrating the stronger dependency of adsorption on the diffusion process. A higher mass transfer of the dye to the adsorbent surface during the initial stages of adsorption was confirmed by the k_{id} value of 0.346 mg·g^{-1}·min$^{-1/2}$. The adsorption amount was smaller in line with diffusion in the second stage, with an R^2 of 0.857 and a lower rate constant of 0.036 mg·g^{-1}·min$^{-1/2}$. This may be because the large-sized dye molecules are traveling slowly and possibly being affected by different repellent forces inside the adsorbent micropores. As a consequence, the intraparticle diffusion mechanism will approach equilibrium slowly in the sorbent's microporous regions, governing bulk adsorption. Based on the aforementioned, the RhB adsorption kinetics onto the biochar/Mn-ZnFe$_2$O$_4$ is now being governed by pseudo-second-order and diffusion-controlled models.

3.2.5. Adsorption Equilibrium. The equilibrium study allows for the evaluation of the developed biochar's adsorption capacity as well as the dye-adsorbent binding strength. Equilibrium experiments were carried out at pH 4.0 with a shaking time of 90 minutes to reach equilibrium, and the initial concentration of RhB ranged from 5 to 100 mg·L^{-1}. A comparison of the experimental data and fitting to the Langmuir and Freundlich isotherms is presented in Figure 11. The experimental data followed a profile very close to the Langmuir isotherms.

To obtain the isotherm parameters, the linear forms of the Langmuir, Freundlich, Tempkin, and Dubinin-Radushkevich (D-R) isotherm models were tested to fit the experimental results. The Langmuir isotherm [39] is expressed by

$$\frac{C_e}{q_e} = \frac{C_e}{q_{max}} + \frac{1}{q_{max} K_L}, \tag{6}$$

where q_e is the adsorbed amount of RhB (mg·g^{-1}) at equilibrium, q_{max} is the maximum adsorbed amount of RhB (mg·g^{-1}) to form a complete monolayer, and C_e is the equilibrium RhB concentration (mg·L^{-1}). K_L stands for the Langmuir constant,
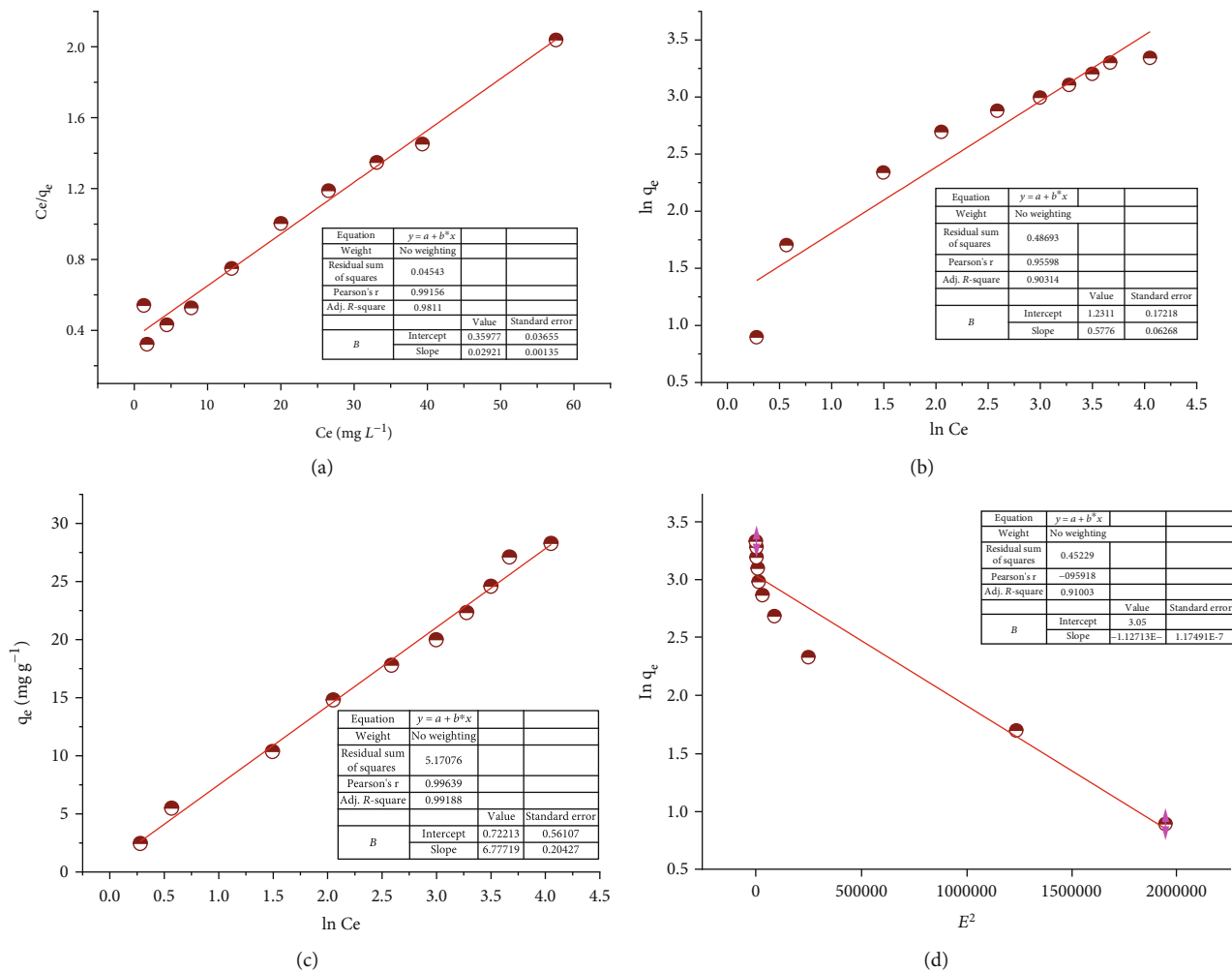
FIGURE 12: The linear plots of the Langmuir (a), Freundlich (b), Tempkin (c), and Dubinin-Radushkevich (d) isotherm models.

which is related to the RhB affinity of binding sites. If this model matches the experimental results, it assumes a monolayer chemical adsorption mechanism. This model could also be used to calculate the maximum monolayer adsorption capacity (q_{max}, mg·g^{-1}). The dimensionless equilibrium constant or separation factor R_L is used to predict favorable adsorption. It is given in Equation (7). Based on the value of R_L, the adsorption isotherm can be classified into linear ($R_L = 1$), favorable ($0 < R_L < 1$), or unfavorable ($R_L > 1$), or irreversible ($R_L = 0$).

$$R_L = \frac{1}{1 + K_L C_e}. \tag{7}$$

The Freundlich isotherm [40], which is an empirical model of heterogeneous surface adsorption, is given by

$$\ln q_e = \left(\frac{1}{n}\right) \ln C_e + \ln K_F, \tag{8}$$

where n and K_F are the Freundlich constants that relate, respectively, to adsorption intensity and capacity.

The adsorbent-adsorbate interaction and heat of adsorption could be evaluated using the Tempkin isotherm model [41] as described by

$$q_e = B \ln A_T + B \ln C_e, \tag{9}$$

where A_T is the Tempkin isotherm equilibrium binding constant (L·g^{-1}) and B is the slope. The Tempkin isotherm constant (b_T) correlated to the heat of adsorption (J·mol^{-1}) is given by

$$B = \frac{RT}{b_T}. \tag{10}$$

The homogeneous surface or a constant adsorption potential is not assumptions made by the Dubinin-Radushkevich (D-R) isotherm model [42] as represented by

$$\ln q_e = \ln X_m - \beta \varepsilon^2. \tag{11}$$

The slope (β) and intercept ($\ln X_\mathrm{m}$) values can be determined by displaying $\ln q_\mathrm{e}$ versus ε^2.

X_m (mol·g^{-1}) denotes the maximum amount of RhB that may be adsorbed onto one gram of the magnetic biochar. The adsorption energy is represented by the constant β (mol^2·J^{-2}). The Polanyi potential (ε) can be calculated by using the following equation:

$$\varepsilon = RT \ln \left(1 + \frac{1}{C_\mathrm{e}} \right), \tag{12}$$

where R is the universal gas constant (8.314 J/mol K) and T is the absolute temperature of 298 Kelvin.

Adsorption free energy (E, KJ·mol^{-1}) is designated as the free energy change when one mole of RhB is transported from the solution infinite to the surface of the adsorbent. Equation (13) can be used to get the value of E.

$$E = \frac{1}{\sqrt{-2\beta}}. \tag{13}$$

The tested isotherm models are plotted in Figures 12(a)–12(d). Also, the calculated isotherm parameters are shown in Table 2. The RhB adsorption was best fitted to the Langmuir model ($R^2 = 0.981$) than the Freundlich with a lower $R^2 = 0.903$. The calculated maximum capacity (q_max) from the Langmuir model was found to be 34.5 mg·g^{-1} which is higher than many other adsorbents such as fly ash [43], Fe-N-co-modified biochar [44], modified zeolite [45], municipal waste biochar [46], and ZnFe$_2$O$_4$-nanocomposite [47]. The high value of q_max ($\gg 1.0$) indicated strong interaction between RhB and the magnetic Biochar, and the removal process proceeded via a monolayer chemical adsorption. Furthermore, the values calculated of separation R_L varied from 0.02 to 0.48 (between $0 > R_\mathrm{L} < 1$), supporting the favorable adsorption of RhB onto the magnetic biochar/Mn-ZnFe$_2$O$_4$. The Freundlich constant K_F was 3.42 L·g^{-1} which shows a stronger affinity of the adsorbent towards RhB. The n constant value was 1.75 ($n > 1$), indicating that the adsorbent has a higher affinity for RhB dye and that cooperative adsorption onto a heterogeneous surface is advantageous. The values of both constants indicated the strong adsorption of RhB by the developed magnetic biochar. This is consistent with the presence of macroporous and mesoporous structures in the SEM micrographs of the magnetic biochar adsorbent. The adsorption process may begin with the RhB diffusion from the bulk of the solution to the sorbent surface and then to the inner surface to combine with active groups for ultimate accumulation in a monolayer pattern.

Figure 12(c) shows the linearized Tempkin adsorption isotherm applied to the experimental results. Good correlation ($R^2 = 0.992$) was higher than that obtained for other isotherms confirming that this isotherm could provide a reasonable model for adsorption. The binding constant A_T was 1.11 L·g^{-1} indicating strong binding between RhB and the adsorbent surface. The Tempkin heat of the adsorption constant, b_T, was equal to 0.37 KJ·mol^{-1}, and constant B had

TABLE 2: Adsorption isotherm parameters for RhB dye adsorption onto P. harmala biochar/Mn-ZnFe2O4.

Isotherm model	Parameter	
Experimental	q_max (mg·g^{-1})	27.7
Langmuir model	q_max (mg·g^{-1})	34.5
	K_L (L·mg^{-1})	0.81
	R_L	0.02-0.48
	R^2	0.981
Freundlich model	n	1.75
	K_F	3.42
	R^2	0.903
Tempkin model	B (J·mol^{-1})	6.80
	A_T (L·g^{-1})	1.11
	b_T (KJ·mol^{-1})	0.37
	R^2	0.992
Dubinin-Radushkevich model	X_m (mg·g^{-1})	21.12
	β (mol^2·J^{-2})	-1.127×10^{-6}
	E (KJ·mol^{-1})	0.67
	R^2	0.910

a positive value of 6.80. This demonstrated that the adsorption is an endothermic process, with a linear increase in adsorption heat as the dye layer thickness on the adsorbent gradually increases. This could be the outcome of stronger dye-biochar/Mn-ZnFe$_2$O$_4$ interaction. The b_T value was rather higher than other adsorbents used for removing RhB such as halloysites [32]. Furthermore, according to this concept, the active sites are distributed uniformly across the magnetic biochar, and there is little evidence of lateral interaction between adsorbed RhB molecules.

A high correlation coefficient ($R^2 = 0.910$) was seen in the D-R model (Figure 12(d)). A heterogeneous microporous structure was visible on the biochar/Mn-ZnFe$_2$O$_4$ surface because the porosity factor (β) was less than 1.0. The maximum adsorption capacity (X_m) estimated is 21.1 mg·g^{-1}, which is less than the maximum capacity of the Langmuir monolayer (q_max). The free energy of adsorption (E) had a positive value of 0.67 kJ·mol^{-1} which emphasized that adsorption is an endothermic chemisorption process. These findings are following the results obtained from the pseudo-second-order kinetic and Langmuir isotherm models.

3.3. Catalytic Removal of RhB. Using the Fenton-like method and hydrogen peroxide (H$_2$O$_2$) as a catalyst for degradation, the degradation of RhB was investigated. The results were compared to the adsorption removal using the adsorbent biochar/Mn-ZnFe$_2$O$_4$ in the absence of H$_2$O$_2$. The results obtained are depicted in Figure 13.

In the absence of H$_2$O$_2$, the results indicated no degradation effect on RhB when using the biochar and magnetic biochar/Fe$_3$O$_4$. This was evidenced by measuring the absorbance of the eluted RhB after adsorption. The removal
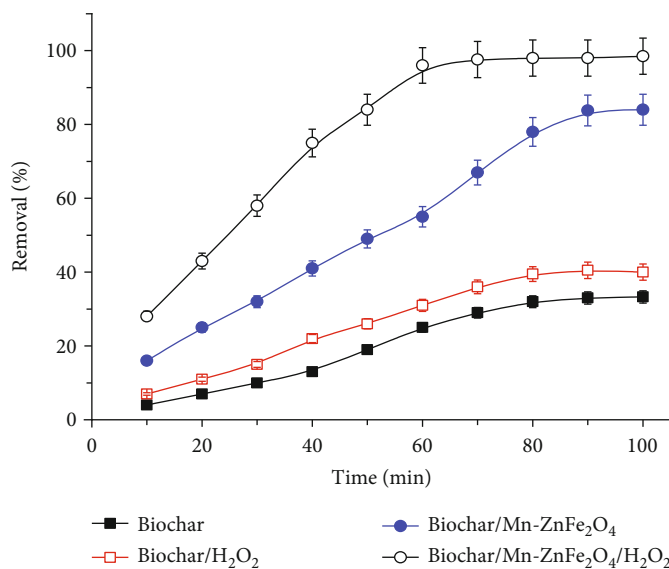
FIGURE 13: Catalytic degradation and adsorption removal of RhB using *P. harmala* biochar and biochar/Mn-ZnFe$_2$O$_4$: 20 mL of 10 mg·L^{-1} RhB solution, pH 4.0, shaking time 10-100 min, adsorbent weight 50 mg, and H$_2$O$_2$ of 0.03% (*v/v*).

TABLE 3: Removal data of RhB dye from industrial wastewater using by adsorption onto P. harmala biochar/Mn-ZnFe$_2$O$_4$ ($n = 4$) and by heterogeneous Fenton catalytic degradation by P. harmala biochar/Mn-ZnFe$_2$O$_4$/H$_2$O$_2$.

RhB added (mg·L^{-1})	Adsorption removal biochar/Mn-ZnFe$_2$O$_4$			Heterogeneous Fenton degradation biochar/Mn-ZnFe$_2$O$_4$/H$_2$O$_2$		
	Remained concentration (*mean ± SD*) (mg·L^{-1})	Removal (%)	RSD (%)	Remained concentration (*mean ± SD*) (mg·L^{-1})	Removal (%)	RSD (%)
5.0	0.85 ± 0.02	83	2.4	0.091 ± 0.007	98	7.6
10.0	2.28 ± 0.13	77	5.7	0.53 ± 0.03	95	5.7

TABLE 4: Adsorption capacity of RhB using different various reported materials.

Adsorbent	pH	Maximum capacity (mg·g^{-1})	Ref.
Biochar/Mn-ZnFe$_2$O$_4$	4.0	34.5	This work
Bamboo biochar	—	85.8	[29]
Fly ash	—	2.33	[43]
Fe-N-co-biochar	—	12.41	[44]
Surfactant-zeolite	8.0	2.03	[45]
Municipal waste biochar	8.7<	20.30	[46]
ZnFe$_2$O$_4$ nanocomposite	4.4	6.02	[47]
Musa biochar	4.0	6.87-7.00	[50]
Gmelina arborea leaf	3.0	1000	[51]

was ≥33 and 84% for biochar and biochar/Mn-ZnFe$_2$O$_4$, respectively.

In the presence of H$_2$O$_2$, the removal reached 40 and 99%, with an increase in the removal by 7 and 15%, respectively. Further, by testing the adsorption in light-exposed and light-protected samples, there was a significant differ-

ence in the adsorbed amount q_e which emphasizes the pronouncing effect of catalytic degradation. Generally, either for biochar or biochar/Mn-ZnFe$_2$O$_4$, the removal profile after the addition of H$_2$O$_2$ is higher than before its addition. Also, the maximal value for removal was reached after shaking of 80 and 70 min for the biochar and biochar/Mn-ZnFe$_2$O$_4$, respectively. There was a 20 min shorter interval than that obtained for biochar/Mn-ZnFe$_2$O$_4$ without the addition of H$_2$O$_2$; it was 90 min. Interpretation of the higher degradation efficiency of the magnetic biochar/Mn-ZnFe$_2$O$_4$ than that of the biochar alone can be due to the electron-rich surface of the magnetic biochar by the existing quinone groups as well as the incorporated ferrite nanoparticles that facilitate the electronic exchange in the oxidation reaction of RhB by the generated hydroxide radicals from H$_2$O$_2$ [48].

In biochar alone, the proposed degradation reaction is a homogeneous catalytic degradation as can be represented by Equations (14)-(16).

$$H_2O_2 + h\nu_{sunlight} ====== 2HO^{\bullet} \qquad (14)$$
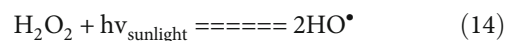
The formed hydroxyl radicals are strong oxidizing agents which can easily oxidize RhB dye to produce an intermediate

TABLE 5: Catalytic degradation removal of RhB using P. harmala biochar/Mn-ZnFe$_2$O$_4$ compared to other materials.

Catalyst	pH	Time (min)	RhB (mg·L^{-1})	Removal (%)	Ref.
P. harmala biochar/Mn-ZnFe$_2$O$_4$/H$_2$O$_2$ (0.03% *v/v*)	4.0	60	100	99	This work
Black liquor-sludge biochar/H$_2$O$_2$ (2 mM)	3.0	10	50	100	[8]
Fe-bentonite/H$_2$O$_2$ (12 mM)	4.2	180	80	93	[52]
Fe/MCM-41/H$_2$O$_2$ (20 mmol)	4.0	30	100	100	[53]
Tin oxide/montmorillonite	—	120	50	100	[54]
Snake fruit peel biochar/H$_2$O$_2$ (0.5%)	7.0	—	—	99.9	[55]

RhB$^{\bullet}$ which decolorizes the parent dye.

$$HO^{\bullet\cdot} + RhB ======= RhB^{\bullet} \text{ dye degradation} \quad (15)$$

Reactions (14) and (15) can occur with biochar in the absence of ferrite nanoparticles and lead to a slight enhancement for dye removal.

The physicochemical properties of the prepared biochar are primarily dependent on the pyrolysis temperature, heating rate, retention time, and chemical pretreatment. The pyrolysis of agricultural waste at 600°C leads to the thermal degradation of hemicellulose, cellulose, and lignin into biosolid, syngas, and biooil. The main superficial functional groups on the surface of biochar (biosolid) are COOH, C=O, OH, and C-O which affect both the adsorption and catalytic degradation of RhB.
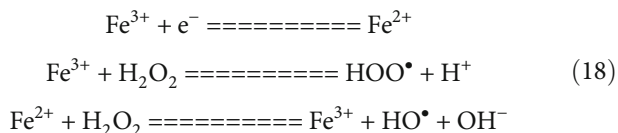
When using the biochar/Mn-ZnFe$_2$O$_4$ heterogeneous Fenton degradation method, the biochar support is deemed to increase the reactivity of the loaded ferrite nanoparticles. The ferrite nanoparticles had the intrinsic peroxidase-like activity that enables Mn-ZnFe$_2$O$_4$ to react with H$_2$O$_2$ to afford the hydroxyl radicals (HO$^{\bullet}$) [49]. The sunlight illumination of the ferrite portion in Mn-ZnFe$_2$O$_4$ permits the UV radiation to react with nanoparticles and producing of electron- (e_{CB}^-) hole (h_{VB}) pairs as shown in

$$Mn - ZnFe_2O_4 + hv_{sunlight} ========== Mn - ZnFe_2O_4(e_{CB} + h_{VB}) \quad (16)$$
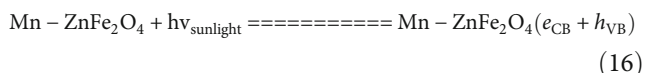
The generated e_{CB} can be captured by H$_2$O$_2$ to produce OH$^{\bullet}$. Also, the photoinduced h_{VB} can react with water or OH$^-$ to furnish hydroxyl radicals:

$$h_{VB} + H_2O ======= OH^{\bullet} + H^+$$
$$h_{VB} + OH^- ======= OH^{\bullet} \quad (17)$$
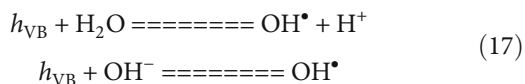
Moreover, the Fe^{3+} ions on the surface of Mn-ZnFe$_3$O$_4$ nanoparticles can react with H$_2$O$_2$ to initiate the Fenton reaction to produce additional HO$^{\bullet}$ radicals as shown by

$$Fe^{3+} + e^- ========= Fe^{2+}$$
$$Fe^{3+} + H_2O_2 ========== HOO^{\bullet} + H^+ \quad (18)$$
$$Fe^{2+} + H_2O_2 ========= Fe^{3+} + HO^{\bullet} + OH^-$$

The enormous amount of HO$^{\bullet}$ produced in the case of biochar/Mn-ZnFe$_2$O$_4$ heterogeneous Fenton degradation is expected to reveal a higher degree of dye degradation and thereby efficient and fast removal than adsorption removal as compared to the biochar alone which had limited sources of radical generation. Worth mentioning, as can be seen in Figure 13, the rate of dye removal was linear in the case of the biochar and biochar/Mn-ZnFe$_2$O$_4$ which indicates that the concentration of H$_2$O$_2$ was suitable for RhB decoloration and the self-quenching of the hydroxyl radicals (HO$^{\bullet}$) was negligible.

3.4. Removal of RhB from Tap and Industrial Wastewater. The developed magnetic biochar was applied to the removal of RhB from industrial wastewater using 50 mg adsorbent, 20 mL spiked wastewater of RhB at concentrations of 5 and 10 mg·L^{-1}, and 0.03% (*v/v*) H$_2$O$_2$. The results obtained are presented in Table 3. The removal ranged from 77 to 83% and from 95 to 98% for biochar/Mn-ZnFe$_2$O$_4$ and biochar/Mn-ZnFe$_2$O$_4$/H$_2$O$_2$, respectively. The precision represented as relative standard deviation (RSD, $n = 4$) at RhB concentration of 5.0 and 10 mg·L^{-1} was 2.4 and 5.7% for biochar/Mn-ZnFe$_2$O$_4$ and 7.6 and 5.7% for biochar/Mn-ZnFe$_2$O$_4$/H$_2$O$_2$, respectively. The average removal was increased after adding H$_2$O$_2$ by a value of 16.5%. This confirmed that adsorption removal is significant and feasible, but the heterogeneous catalytic degradation was a powerful mechanism. Therefore, a combination of the two mechanisms can be preferred in samples which may counteract the removal by applying a single approach.

4. Comparison to Other RhB Removal Adsorbents

The adsorption capacity of P. harmala biochar/Mn-ZnFe2O4 was compared to other reported adsorbents in Table 4. The developed magnetic biochar had a higher capacity than other reported biochars [44, 46, 50] and other adsorbents [43, 45, 47] for the removal of RhB. Despite this, some other plant biomass such as *Gmelina arborea* leaf powder [51] showed extremely higher RhB adsorption capacity than the present material. The obtained capacity is primarily dependent on the method of preparation, pyrolysis temperature, heating rate, and retention time, so it can vary to some extent at other preparation conditions. Despite this, the capacity obtained is sufficient for RhB removal from natural waters. Table 5 compares the developed magnetic biochar's catalytic degradation removal effectiveness to that of other

catalysts. The removal was superior to Fe-bentonite/H_2O_2 [52] in terms of heterogeneous Fenton catalytic degradation and comparable other listed materials. Thus, the developed magnetic biochar proved to be an alternative and suitable for the adsorption and catalytic removal of RhB from a water sample.

5. Conclusions

The magnetic biochar was prepared by a one-step impregnation pyrolysis under nitrogen at 600°C of P. harmala plant powder pretreated with $MnCl_2$, $ZnCl_2$, and $FeCl_3$. The FT-IR analysis showed that the characteristic bands for metal oxide appeared at 543 and 591 cm^{-1}. The XRD pattern showed the crystalline structure of Mn-$ZnFe_2O_4$ embedded in the biochar matrix. The microstructure of the prepared magnetic biochar had higher porosity. The adsorption isotherm was best fitted with the Langmuir model ($R^2 = 0.981$) and Tempkin ($R^2 = 0.992$), and the separation factor R_L ranged from 0.02 to 0.48 confirming a favorable chemical adsorption process. The monolayer adsorption capacity of 34.5 mg·g^{-1} was obtained at pH 4.0, a shaking time of 90 min, and an adsorbent dosage of 3.2 g·L^{-1}. The adsorption kinetics adopted pseudo-second-order kinetic and diffusion-controlled models confirming that diffusion is a rate-limiting step. Heterogeneous Fenton degradation using 0.03% (v/v) H_2O_2 showed enhancement of recovery from 33 to 40% and from 84 to 99% for biochar alone and biochar/Mn-$ZnFe_2O_4$, respectively. The wastewater application showed RhB removal ranged from 77 to 88% and 95 to 98% for biochar/Mn-$ZnFe_2O_4$ and biochar/Mn-$ZnFe_2O_4$/H_2O_2 methods, respectively.

Data Availability

The authors can provide the available data on request after the publication of this article, which will be considered by the corresponding author.

Conflicts of Interest

The authors declare no potential conflict of interest.

Authors' Contributions

Abdulrahman F. Alharbi was responsible for the material characterization and reviewed and edited the manuscript. Abdullah A. Alotaibi was responsible for the conceptualization, resources, and supervision and reviewed and edited the manuscript. Hassan E. M. Gomaa was responsible for the data curation and resources and reviewed and edited the manuscript. Abdulaziz A. M. Abahussain reviewed and edited the manuscript. Sami M. Abdel Azeem was responsible for the conceptualization, data curation, project administration, and funding acquisition and wrote, reviewed, and edited the manuscript.

References

[1] K. Rachna, A. Agarwal, and N. B. Singh, "Preparation and characterization of zinc ferrite–polyaniline nanocomposite for removal of rhodamine B dye from aqueous solution," *Environmental Nanotechnology, Monitoring & Management*, vol. 9, pp. 154–163, 2018.

[2] S. Daniel and U. S. Shoba, "Synthesis, characterization and adsorption behavior of MgO nano particles on rhodamine B dye," *Journal of Chemical and Pharmaceutical Research*, vol. 7, pp. 713–723, 2015.

[3] A. Baddouh, B. El Ibrahimi, E. Amaterz, M. Mohamed Rguiti, L. Bazzi, and M. Hilali, "Removal of the rhodamine B dye at Ti/Ru$_{0.3}$Ti$_{0.7}$O$_2$ anode using flow cell system," *Journal of Chemistry*, vol. 2019, Article ID 1424797, 10 pages, 2019.

[4] Y. Huang, X. Zheng, S. Feng, Z. Guo, and S. Liang, "Enhancement of rhodamine B removal by modifying activated carbon developed from *Lythrum salicaria* L. with pyruvic acid," *Colloids and Surfaces A: Physicochemical and Engineering Aspects*, vol. 489, pp. 154–162, 2016.

[5] R. Jain, M. Mathur, S. Sikarwar, and A. Mittal, "Removal of the hazardous dye rhodamine B through photocatalytic and adsorption treatments," *Journal of Environmental Management*, vol. 85, no. 4, pp. 956–964, 2007.

[6] C. Maria Magdalane, K. Kaviyarasu, J. Judith Vijaya et al., "Evaluation on the heterostructured CeO$_2$/Y$_2$O$_3$ binary metal oxide nanocomposites for UV/Vis light induced photocatalytic degradation of rhodamine - B dye for textile engineering application," *Journal of Alloys and Compounds*, vol. 727, pp. 1324–1337, 2017.

[7] R. Jinisha, R. Gandhimathi, S. T. Ramesh, P. V. Nidheesh, and S. Velmathi, "Removal of rhodamine B dye from aqueous solution by electro-Fenton process using iron-doped mesoporous silica as a heterogeneous catalyst," *Chemosphere*, vol. 200, pp. 446–454, 2018.

[8] J. Xia, Y. Shen, H. Zhang, X. Hu, M. Manik Mian, and W.-H. Zhang, "Synthesis of magnetic nZVI@biochar catalyst from acid precipitated black liquor and Fenton sludge and its application for Fenton-like removal of rhodamine B dye," *Industrial Crops and Products*, vol. 187B, article 115449, 2022.

[9] S. Y. Lee, D. Kang, S. Jeong, H. T. Do, and J. H. Kim, "Photocatalytic degradation of rhodamine B dye by TiO$_2$ and gold nanoparticles supported on a floating porous polydimethylsiloxane sponge under ultraviolet and visible light irradiation," *ACS Omega*, vol. 5, no. 8, pp. 4233–4241, 2020.

[10] M. Gören, H. B. Murathan, N. Kaya, and A. M. Murathan, "Removal of rhodamine B from aqueous solution by using pine cone activated with HNO3," *Journal of International Environmental Application and Science*, vol. 16, pp. 123–132, 2021, https://dergipark.org.tr/en/pub/jieas/issue/65167/991499.

[11] S. A. Mousavi, B. Kamarehie, A. Almasi et al., "Removal of rhodamine B from aqueous solution by stalk corn activated carbon: adsorption and kinetic study," *Biomass Conversion and Biorefinery*, vol. 13, no. 9, pp. 7927–7936, 2023.

[12] S. Khamparia and D. Jaspal, "Investigation of adsorption of rhodamine B onto a natural adsorbent *Argemone mexicana*," *Journal of Environmental Management*, vol. 183, Part 3, pp. 786–793, 2016.

[13] L. Laysandra, M. W. M. K. Sari, F. E. Soetaredjo et al., "Adsorption and photocatalytic performance of bentonite-titanium dioxide composites for methylene blue and rhodamine B decoloration," *Heliyon*, vol. 3, no. 12, p. e00488, 2017.

[14] Z. L. Cheng, Y.-X. Li, and Z. Liu, "Fabrication of graphene oxide/silicalite-1 composites with hierarchical porous structure and investigation on their adsorption performance for rhodamine B," *Journal of Industrial and Engineering Chemistry*, vol. 55, pp. 234–243, 2017.

[15] M. Ptaszkowska-Koniarz, J. Goscianska, and R. Pietrzak, "Removal of rhodamine B from water by modified carbon xerogels," *Colloids and Surfaces A: Physicochemical and Engineering Aspects*, vol. 543, pp. 109–117, 2018.

[16] T. H. Y. Doan, T. P. M. Chu, T. D. Dinh et al., "Adsorptive removal of rhodamine B using novel adsorbent-based surfactant- modified alpha alumina nanoparticles," *Journal of Analytical Methods in Chemistry*, vol. 2020, Article ID 6676320, 8 pages, 2020.

[17] M. Tripathi, J. N. Sabu, and P. Ganesan, "Effect of process parameters on production of biochar from biomass waste through pyrolysis: a review," *Renewable and Sustainable Energy Reviews*, vol. 55, pp. 467–481, 2016.

[18] Y. Chen, Y.-C. Lin, S.-H. Ho, Y. Zhou, and N. Ren, "Highly efficient adsorption of dyes by biochar derived from pigments-extracted macroalgae pyrolyzed at different temperature," *Bioresource Technology*, vol. 259, pp. 104–110, 2018.

[19] I. I. Albanio, P. C. L. Muraro, and W. L. da Silva, "Rhodamine B dye adsorption onto biochar from olive biomass waste," *Water, Air, and Soil Pollution*, vol. 232, no. 5, p. 214, 2021.

[20] Y. Lu, J. Chen, L. Zhao, Z. Zhou, C. Qiu, and Q. Li, "Adsorption of rhodamine B from aqueous solution by goat manure biochar: kinetics, isotherms, and thermodynamic studies," *Polish Journal of Environmental Studies*, vol. 29, no. 4, pp. 2721–2730, 2020.

[21] B. M. Córdova, J. P. S. Cruz, T. V. M. Ocampo, R. G. Huamani-Palomino, and A. M. Baena-Moncada, "Simultaneous adsorption of a ternary mixture of brilliant green, rhodamine B and methyl orange as artificial wastewater onto biochar from cocoa pod husk waste. Quantification of dyes using the derivative spectrophotometry method," *New Journal of Chemistry*, vol. 44, no. 20, pp. 8303–8316, 2020.

[22] Z. Jiang, Y. Zhao, and P. Yang, "Formation of MFe2O4 (M = Co, Mn, Ni) 1D nanostructures towards rapid removal of pollutants," *Materials Chemistry and Physics*, vol. 214, pp. 1–7, 2018.

[23] E. S. Ngankam, L. Dai-Yang, B. Debina, A. Baçaoui, A. Yaacoubi, and A. N. Rahman, "Preparation and characterization of magnetic banana peels biochar for Fenton degradation of methylene blue," *Materials Sciences and Applications*, vol. 11, no. 6, pp. 382–400, 2020.

[24] H. Zhang, G. Xue, H. Chen, and X. Li, "Magnetic biochar catalyst derived from biological sludge and ferric sludge using hydrothermal carbonization: preparation, characterization and its circulation in Fenton process for dyeing wastewater treatment," *Chemosphere*, vol. 191, pp. 64–71, 2018.

[25] M. M. Zhang, Y. G. Liu, T. T. Li et al., "Chitosan modification of magnetic biochar produced from *Eichhornia crassipes* for enhanced sorption of Cr(VI) from aqueous solution," *RSC Advances*, vol. 5, no. 58, pp. 46955–46964, 2015.

[26] Z. Niu, W. Feng, H. Huang et al., "Green synthesis of a novel Mn-Zn ferrite/biochar composite from waste batteries and pine sawdust for Pb^{2+} removal," *Chemosphere*, vol. 252, article 126529, 2020.

[27] A. Nasiri, S. Rajabi, and M. Hashimi, "$CoFe_2O_4$@methylcellulose/ AC as a new, green, and eco-friendly nano-magnetic adsorbent for removal of Reactive Red 198 from aqueous solution," *Arabian Journal of Chemistry*, vol. 15, no. 5, article 103745, 2022.

[28] N. Danesh, M. Ghorbani, and A. Marjani, "Separation of copper ions by nanocomposites using adsorption process," *Scientific Reports*, vol. 11, no. 1, p. 1676, 2021.

[29] Y. Hou, G. Huang, J. Li, Q. Yang, S. Huang, and J. Cai, "Hydrothermal conversion of bamboo shoot shell to biochar: preliminary studies of adsorption equilibrium and kinetics for rhodamine B removal," *Journal of Analytical and Applied Pyrolysis*, vol. 143, article 104694, 2019.

[30] S. M. A. Azeem, M. M. S. Wahsh, F. H. Youssef, A. M. H. Ibrahim, and N. Burham, "Magnetic nanocomposite of zinc–manganese ferrite/polyurethane foam for adsorption of copper and cadmium from water," *Desalination and Water Treatment*, vol. 267, pp. 26–44, 2022.

[31] R. C. Pawar, V. Khare, and C. S. Lee, "Hybrid photocatalysts using graphitic carbon nitride/cadmium sulfide/reduced graphene oxide (g-C3N4/CdS/RGO) for superior photodegradation of organic pollutants under UV and visible light," *Dalton Transactions*, vol. 43, no. 33, pp. 12514–12527, 2014.

[32] E. Wierzbicka, K. Kusmierek, A. Swiatkowski, and I. Legocka, "Efficient rhodamine B dye removal fromwater by acid- and organo-modified halloysites," *Minerals*, vol. 12, no. 3, p. 350, 2022.

[33] Y. Yu, B. N. Murthy, J. Shapter, K. T. Constantopoulos, N. Voelcker, and A. Ellis, "Benzene carboxylic acid derivatized graphene oxide nanosheets on natural zeolites as effective adsorbents for cationic dye removal," *Journal of Hazardous Materials*, vol. 260, pp. 330–338, 2013.

[34] H. Li, H. Ji, X. Cui et al., "Kinetics, thermodynamics, and equilibrium of As(III), Cd(II), Cu(II) and Pb(II) adsorption using porous chitosan bead-supported $MnFe_2O_4$ nanoparticles," *International Journal of Mining Science and Technology*, vol. 31, no. 6, pp. 1107–1115, 2021.

[35] U. Jinendra, D. Bilehal, B. M. Nagabhushana, and A. P. Kumar, "Adsorptive removal of rhodamine B dye from aqueous solution by using graphene- based nickel nanocomposite," *Heliyon*, vol. 7, no. 4, article e06851, 2021.

[36] Y. S. Ho and G. McKay, "Sorption of dye from aqueous solution by peat," *Chemical Engineering Journal*, vol. 70, no. 2, pp. 115–124, 1998.

[37] Y. S. Ho, D. A. J. Wase, and C. F. Forster, "Study of the sorption of divalent metal ions on to peat," *Adsorption Science and Technology*, vol. 18, no. 7, pp. 639–650, 2000.

[38] W. J. Morris and C. Weber, "Kinetics of adsorption on carbon from solution," *Journal of the Sanitary Engineering Division*, vol. 89, no. 2, pp. 31–59, 1963.

[39] I. Langmuir, "The adsorption of gases on plane surfaces of glass, mica and platinum," *Journal of the American Chemical Society*, vol. 40, no. 9, pp. 1361–1403, 1918.

[40] H. M. F. Freundlich, "Over the adsorption in solution," *The Journal of Physical Chemistry*, vol. 57, pp. 385–470, 1906.

[41] M. Kondalkar, U. Fegade, S. K. Inamuddin, K. Altalhi, K. E. Suryawanshi, and A. M. Patil, "Adsorption of Cr(VI) on ultrafine Al2O3-doped $MnFe_2O_4$ nanocomposite surface: experimental

and theoretical study using double-layer modeling," *Journal of Physics and Chemistry of Solids*, vol. 163, article 110544, 2022.

[42] N. S. Ammar, N. A. Fathy, H. S. Ibrahim, and S. M. Mousa, "Micro-mesoporous modified activated carbon from corn husks for removal of hexavalent chromium ions," *Applied Water Science*, vol. 11, no. 9, p. 154, 2021.

[43] T. A. Khan, I. Ali, V. V. Singh, and S. Sharma, "Utilization of fly ash as low-cost adsorbent for the removal of methylene blue, malachite green and rhodamine B dyes from textile wastewater," *Journal of Environmental Protection Science*, vol. 3, pp. 11–22, 2009.

[44] X. Li, J. Shi, and X. Luo, "Enhanced adsorption of rhodamine B from water by Fe-N co-modified biochar: preparation, performance, mechanism and reusability," *Bioresource Technology*, vol. 343, article 126103, 2022.

[45] R. R. Alcântara, R. O. R. Muniz, and D. A. Fungaro, "Full factorial experimental design analysis of rhodamine B removal from water using organozeolite from coal bottom ash," *International Journal of Energy and Environment*, vol. 7, no. 2016, pp. 357–374, 2016.

[46] I. Ibrahim, S. B. Batagarawa, and A. Salisu, "Adsorption studies of rhodamine b dye from aqueous solution using alkaline modified biochar & non modified biochar obtained from the pyrolysis of municipal solid waste," *Fudma Journal of Sciences*, vol. 5, pp. 334–341, 2022.

[47] W. Konicki, D. Siber, and U. Narkiewicz, "Removal of rhodamine B from aqueous solution by $ZnFe_2O_4$ nanocomposite with magnetic separation performance," *Polish Journal of Chemical Technology*, vol. 19, no. 4, pp. 65–74, 2017.

[48] F. Keyhanian, S. Shariati, M. Faraji, and M. Hesabi, "Magnetite nanoparticles with surface modification for removal of methyl violet from aqueous solutions," *Arabian Journal of Chemistry*, vol. 9, pp. S348–S354, 2016.

[49] F. Ajormal, F. Moradnia, S. T. Fardood, and A. Ramazani, "Zinc ferrite nanoparticles in photo-degradation of dye: mini-review," *Journal of Chemical Reviews*, vol. 2, no. 2, pp. 90–102, 2020.

[50] F. A. Adekola, S. B. Ayodele, and A. A. Inyinbor, "Efficient rhodamine B removal using acid and alkaline-activated Musa paradisiaca biochar," *Polish Journal of Environmental Studies*, vol. 28, no. 5, pp. 3063–3070, 2019.

[51] O. S. Bello, E. O. Alabi, K. A. Adegoke, S. A. Adegboyega, A. A. Inyinbor, and A. O. Dad, "Rhodamine B dye sequestration using *Gmelina aborea* leaf powder," *Heliyon*, vol. 6, no. 1, article e02872, 2020.

[52] D. Xu, X. Sun, X. Zhao et al., "Heterogeneous Fenton degradation of rhodamine B in aqueous solution using Fe-loaded mesoporous MCM-41 as catalyst," *Water, Air, and Soil Pollution*, vol. 229, no. 10, p. 317, 2018.

[53] Y. Gao, Y. Wang, and H. Zhang, "Removal of rhodamine B with Fe-supported bentonite as heterogeneous photo- Fenton catalyst under visible irradiation," *Applied Catalysis B: Environmental*, vol. 178, pp. 29–36, 2015.

[54] I. Fatimah, R. Nurillahi, I. Sahroni et al., "Sonocatalytic degradation of rhodamine B using tin oxide/montmorillonite," *Journal of Water Process Engineering*, vol. 37, article 101418, 2020.

[55] I. Fatimah, G. Purwiandono, I. Sahroni et al., "Magnetically-separable photocatalyst of magnetic biochar from snake fruit peel for rhodamine B photooxidation," *Environmental Nanotechnology, Monitoring & Management*, vol. 17, article 100669, 2022.